Hooked flare ribbons and flux-rope related QSL footprints

Jie Zhao, Stuart Gilchrist, Guillaume Aulanier, Brigitte Schmieder, Etienne Pariat, Hui Li

Hooked flare ribbons and flux-rope related QSL footprints

Jie Zhao[1], **Stuart A. Gilchrist**[2,3], Guillaume Aulanier[2], Brigitte Schmieder[2], Etienne Pariat[2], Hui Li[1]

nj.lihui@pmo.ac.cn

Received _____; accepted _____

[1]Key Laboratory of Dark Matter and Space Astronomy, Purple Mountain Observatory, CAS, Nanjing 210008, China

[2]LESIA, Observatoire de Paris, PSL Research University, CNRS, Sorbonne Universités, UPMC Univ. Paris 06, Univ. Paris-Diderot, Sorbonne Paris Cité, 5 place Jules Janssen, F-92195 Meudon, France

[3]NorthWest Research Associates, 3380 Mitchell Lane, Boulder, CO 80301, USA

ABSTRACT

We studied the magnetic topology of active region 12158 on 2014 September 10 and compared it with the observations before and early in the flare which begins at 17:21 UT (SOL2014-09-10T17:45:00). Our results show that the sigmoidal structure and flare ribbons of this active region observed by **SDO/AIA** can be well reproduced from a Grad-Rubin non linear force free field extrapolation method. Various inverse-S and -J shaped magnetic field lines, that surround a coronal flux rope, coincide with the sigmoid as observed in different extreme ultraviolet wavelengths, including its multi-threaded curved ends. **Also,** the observed distribution of surface currents in the magnetic polarity where it was not prescribed is well reproduced. This validates our numerical implementation and set-up of the Grad-Rubin method. The **modeled** double inverse-J shaped Quasi-Separatrix Layer (QSL) footprints match the observed flare ribbons during the rising phase of the flare, including their hooked parts. The spiral-like shape of the latter may be related to a complex pre-eruptive flux rope **with** more than one turn of twist, as obtained in the model. These ribbon-associated flux-rope QSL-footprints are consistent with the new standard flare model in **3D**, with the presence of a hyperbolic flux tube located below an inverse **tear drop shaped** coronal QSL. This is a new step forward forecasting the **locations of reconnection and ribbons** in solar flares, and the geometrical properties of eruptive flux ropes.

Subject headings: Sun: magnetic fields – Sun: flares – Sun: chromosphere

1. Introduction

Solar flares are the most violent examples of solar activity. Eruptive flares accompany Coronal Mass Ejections (CMEs) and are statistically the most energetic type of flares (Yashiro et al. 2005; Wang & Zhang 2007). Although their pre-eruptive configuration and initiation mechanisms in three dimensions have been studied for many years (see e.g. the modeling of Régnier & Amari 2004 and Amari et al. 2014, as well as the reviews of Aulanier 2014; Janvier et al. 2015; Schmieder et al. 2015 with their accompanying references), a standard model for eruptive flare has not yet been well established. The old CSHKP model in two dimensions (Carmichael 1964; Sturrock 1966; Hirayama 1974; Kopp & Pneuman 1976) remains an influential model that is often described as a "standard" model of eruptive flares. In this model, the flare is powered by magnetic reconnection at a vertical current sheet that forms in the corona below a detached, upward-propagating plasmoid representing the CME. Particles accelerated in the reconnection region travel along the magnetic field to the Sun's surface. At the surface, the particles heat the plasma causing the development of two bright flare ribbons at the footpoints of magnetic separatrix field lines, which correspond to the reconnecting field lines. In the CSHKP picture, the two ribbons are straight lines that are parallel to the polarity inversion line (PIL) and move away from each other as the flare proceeds. Over the years, this general picture has been found to be consistent with most observations, and has been extremely successful in explaining the so-called two-ribbon flares. However, key elements that are missing in the 2D CSHKP model are the shape, location, and dynamics of the ribbons, most particularly their extremities, and their link with the legs of the three dimensional (3D) erupting flux rope.

The issues with the CSHKP model were first addressed by a series of 3D models that consider a non-force-free flux rope embedded in simple magnetic arcade (Démoulin et al. 1996). In these models, the ribbons coincide with the photospheric footprint of a

Quasi-Separatrix Layer (QSL) that encloses the flux rope. The extremities of the ribbons are hook shaped for weakly twisted flux ropes and are spiral shaped for highly twisted flux ropes.

Later studies have shown that the QSLs of more realistic flux ropes are also hook shaped. Titov (2007) and Pariat & Démoulin (2012) analyze the analytic nonlinear force-free-field (NLFFF) flux rope model of Titov & Démoulin (1999). We illustrate in Figure 1 (adapted from Pariat & Démoulin 2012) the aforementioned shapes for the hooks of the QSL footprints associated with flux ropes of various twists. In this Figure, panels (a) and (b) show the hook-shaped QSLs for flux ropes with a moderate twist of 1 and 1.5 turns respectively. Panel (c) shows the spiral-shaped QSLs for a highly twisted flux rope with 2 turns. In all three cases the QSLs wrap around the legs of the rope. Schrijver et al. (2011) and Janvier et al. (2013) analyze the flux-cancellation magneto-hydrodynamical simulations of Aulanier et al. (2010) and Aulanier et al. (2012) respectively. Savcheva et al. (2012a,b) analyze a NLFFF model of an observed sigmoid. Their model is constructed using the flux-insertion magneto-frictional method (van Ballegooijen 2004). Although the flux ropes are constructed in different ways, J-shaped QSL-hooks are always present around their intersection with the photosphere.

The idea that flare ribbons appear at the QSL footprints is also supported by the identification of pairs of J-shaped ribbons in a handful of observed eruptive flares that resemble the hooked QSL footprints from the topological studies (e.g., Chandra et al. 2009, Schrijver et al. 2011).

The results of the topological studies have inspired a new model that extends the CSHKP model to 3D. The model is presented in a series of papers (Aulanier et al. 2012, 2013; Janvier et al. 2013) and is discussed in the review of Janvier et al. (2015). The model makes specific predictions regarding the geometry of the pre-eruption magnetic field. In

particular, it predicts the presence of a particular magnetic structure called a Hyperbolic Flux Tube (HFT) in the corona (Titov et al. 2002). The HFT is formed by intersecting QSLs and is the predicted site of flare reconnection. The footprints of the HFT at the photosphere are the locations of the flare ribbons, which are hook shaped in the model.

This model is now being consolidated by new results. As one example, Savcheva et al. (2012a,b) find QSLs with a tear-drop geometry and an HFT a few moments before the onset of the eruption of a long-lived sigmoid, by using the flux-rope insertion method. As another example, Zhao et al. (2014) find an HFT in a reconstruction of the coronal magnetic field before a major flare on 2011 February 15 (Schrijver et al. 2011; Sun et al. 2012), by using the Optimization method as first introduced by Wheatland et al. (2000) and further developed by Wiegelmann (2004). In addition, again using the flux-rope insertion method, Savcheva et al. (2015) construct NLFFF models for no less than seven sigmoids, with hooked-shaped QSL footprints, that eventually developed into eruptive flares. The authors show, however, that it is particularly difficult to reproduce the location of the hooked parts of the J-shaped ribbons, and therefore to accurately model the flux rope endpoints (Savcheva et al. 2016).

These recent developments, however, may be questioned because the models cited here all suffer from different limitations. The Titov-Démoulin (hereafter TD) NLFFF model is analytical, symmetric and idealized. The flux-cancellation MHD models are also idealized and their flux-rope geometry depends on some observational-inspired (although still parameterized) boundary driving. The Optimization-related NLFFF comprises a low-altitude flux rope before the eruption, which is different from the other NLFFF model (Inoue et al. 2015) for the same event. The relative merits of the latter two approaches are difficult to establish since the pre-eruptive sigmoid is poorly observed. The flux-insertion method that was used to model a large number of sigmoids does not use the observed vector magnetogram data as boundary conditions. Instead, the method uses line-of-sight

magnetogram data combined with a parameterized insertion of axial and poloidal magnetic flux in the corona. The magnitude of the inserted flux, and the shape and length of the insertion region are free parameters of the method that are adjusted by a trial-and-error procedure. The trial-and-error procedure also includes user-driven comparison of the models with coronal observations (UV and X-rays images) to determine the best-suited model.

In this paper, we aim to test the association between QSLs and flare ribbons (especially at the hook parts) by modeling the coronal magnetic field of an eruptive sigmoid using the Grad-Rubin method. This method uses the observed vector magnetic field at the photosphere to construct the coronal magnetic field using a nonlinear force-free model. Although there are a number of methods for constructing NLFFF (see reviews by Aly 1989; Wiegelmann 2008; Wiegelmann & Sakurai 2012; Régnier 2013), the Grad-Rubin method is the only one based on a well-posed boundary value problem. This method has been able to reconstruct twisted flux ropes and reproduce sigmoids as observed in X-rays (Régnier & Amari 2004; Canou et al. 2009; Canou & Amari 2010). In addition, the method has been shown to be one of the best methods in terms of satisfying the solenoidal condition for magnetic fields (see DeRosa et al. 2009 for a comparison of methods). Unlike other methods, the Grad-Rubin method is based on a well-posed boundary value problem and does not unavoidably introduce a finite divergence when observed boundary conditions are imposed. In this paper, the NLFFF calculation is done in spherical geometry using the recently developed Current-Field Iteration in Spherical Coordinates (CFITS) code (Gilchrist & Wheatland 2014).

We consider the sigmoid that was observed in extreme ultraviolet (EUV) with the *Solar Dynamics Observatory* (*SDO;* Pesnell et al. 2012), within the NOAA AR 12158, on 2014 September 10. Our choice for this event is motivated by the recent report of so-called slipping reconnection during the eruption, as evidenced by loop displacements along the

J-shaped ends of the flare ribbons (Li & Zhang 2015). This slipping behavior corresponds to the regime under which reconnection takes place in QSLs in general (Aulanier et al. 2006) and in MHD simulations of erupting sigmoids in particular (Janvier et al. 2013). This event occurs within a bipolar magnetic environment that is simpler than that of the few other similar events previously reported (Li & Zhang 2014).

Our study has two objectives. The first is to test if the Grad-Rubin method in general, and the CFITS code in particular, can reproduce all the following observational features: the sigmoid, the flare ribbons and their J-shaped extremities, and the photospheric current distribution, especially within the polarity where the observed currents are not prescribed as boundary conditions (see discussion in Wheatland & Régnier 2009). The second is to test the robustness of earlier findings, and to assess whether the 3D model proposed by Janvier et al. (2015) can be qualified as standard or not.

The paper is organized as follows: In Section 2 we present the observations of the sigmoid of AR 12158. In Section 3 we present the results of the NLFFF extrapolation. In Section 4 we compare the magnetic topology obtained from the extrapolation and the flare ribbons. In Section 5 we discuss the results. In Section 6 we give a summary and conclusion.

2. Observations

NOAA AR 12158 rotated onto the disk around 2014 September 3. In the days leading up to the eruption on September 10, the region was bipolar and consisted of a single large spot surrounded by plage. Panel (a) of figure 2 shows the radial magnetic field of the region derived from an Helioseismic and Magnetic Imager (HMI) magnetogram (Scherrer et al. 2012) taken on September 10 at 15:24 UT (about two hours before the eruption). The

image shows that the central spot is positive and is flanked by a diffuse region of negative field to the south. Panel (b) shows the radial electric current density J_r for the region derived from the curl of the HMI vector magnetic field at the same time. A concentrated arc of negative J_r dominates the positive spot (shown by the arrow $A1$). The current over the negative polarity is generally diffuse, with a single strong concentration to the east of the main spot (indicated by the arrow $C1$).

The region was observed by the *Atmospheric Imaging Assembly* (AIA) onboard *SDO* (Lemen et al. 2012) and in soft X-rays (SXR) with the *X-Ray Telescope* (XRT; Golub et al. 2007) instrument on Hinode (Kosugi et al. 2007). We are primarily interested in the reconstruction of the sigmoid on September 10. There it is primarily visible in the three specific EUV channels at 94 Å, 131 Å, and 335 Å(see top panels of Figure 3) as well as in SXR. We do not show the latter in this paper because, for this particular sigmoid, the features that are visible in SXR are very similar to those observed in 94 Å(where the sigmoid is also more prominent than in all the other EUV channels of AIA.) The sigmoid has an inverse-S shape and it displays several individual loops and substructures.

Numerical simulations of sigmoid formation and eruption (Amari et al. 2014), of kink (Kliem et al. 2004) and torus (Aulanier et al. 2010) instabilities of solar-like flux ropes, and of the distribution of their electric currents (Török et al. 2014; Dalmasse et al. 2015) all **together** suggest that sigmoids are formed by the ensemble of the double-J shaped arcades in sheared magnetic fields, and that when those arcades reconnect, they turn into fully S-shaped loops which progressively build-up a flux rope. In the frame of these models, the sigmoid has the same handedness with the flux rope, **i.e.** the inverse-S shape is associated with a left-handed twist and a negative helicity, and the electric current density **J** in the center of the flux rope is anti-parallel to the **magnetic** field **B**. The distribution of J_r and B_r as **observed** near the sigmoid ends (**the regions** that primarily **display** $J_r\ B_r \leq 0$, see

Figure 2) is consistent with this scenario.

On 2014 September 10, the sigmoid erupted producing an X1.6 class flare and a CME[1]. Based on the GOES 1−8 Å soft X-ray light curve, the flare begins at 17:21 UT, reaches its peak at 17:45 UT, and ends at 18:20 UT. This event is the focus of several observational studies: Cheng et al. (2015) performs a spectroscopic study of the sigmoid and the flare ribbons, while Li & Zhang (2015) reports the observation of slip-running reconnection that Dudik et al. (2016) investigate in more detail. The Solar Object Locator (SOL) for this event is SOL2014-09-10T17:45:00.

3. Nonlinear Force-free extrapolation of AR 12158

We construct a NLFFF model of the coronal magnetic field of AR 12158 using the Current-Field Iteration in Spherical Coordinates code (CFITS) (Gilchrist & Wheatland 2014). The code is a numerical implementation of the Grad-Rubin method (Grad & Rubin 1958) in spherical coordinates different from the one developed by Amari et al. (2013). The present study is the first time the CFITS code has been applied to solar data rather than test cases (Gilchrist & Wheatland 2014).

NLFFF modeling of the corona is the subject of multiple reviews (Wiegelmann 2008; Wiegelmann & Sakurai 2012), so we only briefly outline the general approach here. The basic assumption is that the magnetic field in the corona, $\mathbf{B}$, exists in a force-free state, i.e. $\mathbf{J} \times \mathbf{B} = 0$, where $\mathbf{J}$ is the electric current density. This condition combined with Ampère's law provides a set of partial-differential equations (the force-free equations) for the magnetic field in the volume (Priest 1982). The equations can be solved subject to boundary conditions on the magnetic field and electric current at the photosphere and other

[1]`http://www.swpc.noaa.gov`

boundaries. The force-free equations are generally nonlinear, and specialized numerical methods are required to solve them (Wiegelmann & Sakurai 2012).

In spherical geometry, the boundary conditions are imposed on a spherical shell of a given radius. We impose boundary conditions on a shell located at $R_\odot$. In practice, the boundary conditions are derived from vector magnetogram data. We note that **these** data **represent** the magnetic field around the height of line formation, which **do** not necessarily correspond to $R_\odot$, but we make the approximation that **the two coincide**. The specific boundary conditions imposed are the normal component of $\mathbf{B}$,

$$B_r|_{r=R_\odot}, \tag{1}$$

and the distribution of the force-free parameter, $\alpha = \mu_0 \mathbf{J} \cdot \mathbf{B}/B^2$, which we take as

$$\alpha_0 = \mu_0 \left. \frac{J_r}{B_r} \right|_{r=R_\odot}, \tag{2}$$

because vector-magnetogram data does not provide the vector-current density $\mathbf{J}$. In fact, to prescribe α_0 everywhere in the boundary is an over specification of the boundary value problem (Grad & Rubin 1958). Instead, α_0 is only prescribed over one polarity of B_r, i.e. we fix α_0 either at points in the boundary where $B_r > 0$ or at points in the boundary where $B_r < 0$. We refer to the two choices as the P and N boundary conditions respectively.

We derive the P and N boundary conditions from vector-magnetogram data from *HMI/SDO*. Specifically, we use data taken at 15:24 UT on September 10 from the 720s Space-Weather HMI Active Region Patch (SHARP) series (Bobra et al. 2014) with HARP number 4536. We determine J_r by computing the curl of the magnetic field at the photosphere after first smoothing the transverse components using a Laplace scheme (Press et al. 2007). The smoothing reduces strong gradients in α_0, which are difficult to resolve numerically in the modeling. In addition, we set $\alpha_0 = 0$ where $|B_r| < 50\,\mathrm{G}$, because the transverse magnetic field is typically poorly measured in weak field regions.

Panels (a)-(c) of Figure 2 shows the distributions of B_r and J_r derived from the HMI data. The data are saturated at the limits indicated by the color bars. Panel (a) shows B_r. Panel (b) shows J_r without any smoothing applied. Panel (c) shows J_r computed after first smoothing the transverse components of the magnetic field. Although the smoothing removes a lot of fine structure, the overall distribution of J_r is left intact. The region is viewed as seen from Earth, and the yellow curve demarcates the extent of the HMI magnetogram at the photosphere. The green and purple lines are the $+200\,\mathrm{G}$ and $-200\,\mathrm{G}$ contours of B_r respectively.

Unlike in the corona, the magnetic field at the photosphere is not force free (Metcalf et al. 1995), which raises concerns about the NLFFF modeling (e.g. DeRosa et al. 2009). This problem is generally treated by pre-processing the vector magnetogram data to minimize forces in the boundary (Wiegelmann et al. 2006). Other methods modify the photospheric boundary data in both polarities during the solution of the force-free equations themselves (Wheatland & Régnier 2009). In either case, the magnitude of α in the boundary is typically reduced. We adopt an alternative approach, and reduce α in the boundary by a parameterization of the boundary conditions. Our parameterization is crude – we simply scale α_0 by a constant factor k. We do not parameterize B_r. The parameterization is chosen to model the decrease in α from the photosphere to the corona (Gosain et al. 2014), although it does not model changes to the spatial distribution of α_0, which are likely important.

In the following, we will refer to the original distribution of α derived from the HMI data before smoothing and scaling as α_0^{raw}, and we refer to the distribution of α after smoothing and scaling as α_0. The latter is used as boundary conditions for the modeling.

For our calculation, we use a spherical-polar coordinate mesh with 256 points in the radial direction, 273 points in latitude, and 304 points in longitude. The grid has a uniform

spacing of 0.7Mm in both latitude and longitude, and a uniform spacing of 1.1 Mm in the radial direction. The grid extents radially to a distance of 0.4 solar radii (≈ 268 Mm) above the photosphere.

We apply CFITS to the P and N boundary conditions. We find that the N solution is close to a potential field — the magnetic energy and the field lines are close to the initial potential field. The N solution does not contain a flux rope, regardless of the degree of smoothing or the choice of the k parameter.

The boundary conditions for the N solution are derived from the HMI observations in a dispersed plage region. There the sizes of network flux-concentrations, as observed at the high-resolution of HMI, are not very large as compared with the pixel size of the instrument. The associated electric current densities, as calculated from Ampère's law, are therefore very fragmented, with little coherent structure on average (even though some current concentrations are still noticeable). As a consequence, the NLFFF extrapolation either becomes intractable, when one wishes to keep such spiky current densities as boundary conditions, or results in a quasi-potential field with only of few regions that display moderately sheared-arcades, when the current densities are smoothed enough to make the calculation feasible. As a result, we discard the N solution and only present the P solution here. The P solution only relies on α_0 values in the positive polarity and so is unaffected by the noise in the negative polarity — this is an advantage of the Grad-Rubin method over methods that prescribe boundary conditions over the entire boundary.

For the P boundary conditions, we perform multiple calculations with different values of k in the range $[0.5 - 1.0]$ and different degrees of smoothing. We have chosen the solution that best matches the aforementioned AIA data to present here. We note that the convergence of the method for $k = 1$ is poor. This can occur in the presence of large electric currents, and has been reported for other Grad-Rubin codes (Gilchrist et al. 2012). The

convergence of the method is generally improved for smaller k, where the solution becomes closer to a potential field, although the resulting field does not closely match the AIA image (we do not present comparisons between these solutions and the AIA images).

Figure 3 (d) - (h) **show** the field lines of the NLFFF model after 30 Grad-Rubin iterations applied to the P boundary conditions with $k = 0.66$. Panels (d)-(f) show the field lines of the solution superimposed on AIA images of the region. The red, yellow, and orange lines show the inverse-S and -J shaped magnetic field lines which appear to trace the sigmoid. The purple field lines show a flux rope. But it has no observational counterpart, **neither in the EUV AIA channels (94 Å, 131 Å, 335 Å)** , nor in the XRT images in SXR. Panels (g) and (h) show three dimensional views of the same sets of field lines in addition to a set of arcade field lines in blue.

For the P solution, we impose boundary conditions on α at points in the photosphere where $B_r > 0$, while the value of α at points in the photosphere where $B_r < 0$ is determine by solving the force-free model. We refer to the distribution of α at the photosphere obtained from the modeling as α_0^P. Generally, where $B_r > 0$, $\alpha_0^P = \alpha_0$, except in open field regions where the code sets $\alpha_0^P = 0$ (Gilchrist & Wheatland 2014). A priori we do not expect $\alpha_0^P = \alpha_0$ where $B_r < 0$, because the distribution α_0 is not consistent with a force-free model, i.e. the model will only **very** approximately recover the magnetogram currents. In addition, since α_0 does not match $\alpha_0^{\rm raw}$ due to smoothing and scaling, a priori we do not expect a close match between α_0^P and $\alpha_0^{\rm raw}$. However the observed distribution of currents over the negative polarities matches well with the reconstructed distribution of currents. This validates our present numerical implementation of the Grad-Rubin method. Panel (d) of Figure 2 shows the radial current density, J_r, constructed from α_0^P. This can be compared with the distributions of J_r in panel (c) which is constructed from α_0. There are noticeable differences between the two distributions, nevertheless, the model recovers

the strong current concentration at $(X, Y) \approx (-150", 150")$. This feature is also present in the unsmoothed data, as indicated by the arrow $C1$ in panel (b). The good correspondence between the modeled α distribution and the observed α distribution suggests our model field is a plausible model of the coronal magnetic field of AR 12158.

To measure the divergence of our solution we compute the metric $\langle |f_i| \rangle$ from Wheatland et al. (2000). This metric measures the flux imbalance over each grid cell averaged over the whole domain. Specifically,

$$f_i = \frac{\int \mathbf{B} \cdot \mathbf{dS}}{\int |\mathbf{B} \cdot \mathbf{dS}|} \tag{3}$$

where the integrals are over the boundaries of each spherical grid cell, and $\langle . \rangle$ denotes the average over all cells in the domain. For our solution we find $\langle |f_i| \rangle \approx 6.5 \times 10^{-4}$. This value, obtained for a highly-stressed magnetic configuration, is comparable to those found in DeRosa et al. (2015) for force-free extrapolations **in** Cartesian coordinates using a variety of methods applied to a much less stressed solar active region (some of which still being able to perform relatively better or worse than this value).

4. Topological analysis and observational comparison

We compute the QSLs of the force-free model obtained from one HMI magnetogram from 15:24 UT for comparison with the observed flare ribbons during the initial rising phase of the flare.

4.1. Topology and QSLs

With the aim of determining the QSLs, we compute the squashing factor Q for the nonlinear force-free model using the formula of Pariat & Démoulin (2012).

The squashing factor is a measure of the gradient in the field line connectivity (Titov et al. 2002), and thin layers where Q is "large" are defined as QSLs. In principle, QSLs are three dimensional. We have chosen two-dimensional slices for comparison with observations and models. For comparison with observations, only the projections of the QSLs at the photosphere are relevant for comparison with the flare ribbons. For comparison with the models, we have computed QSLs on a slice through the flux rope in order to identify the Hyperbolic Flux Tube (HFT) and compare with similar QSL calculations made with model flux ropes. This kind of comparison has already been achieved in earlier studies of NLFFF models of sigmoids (Savcheva et al. 2012a, 2015, 2016; Zhao et al. 2014). QSLs have rarely been computed in three dimensions (see e.g. Yang et al. 2015), and to the authors' knowledge this has been achieved for flux rope models only in the case of one analytical TD rope (Titov 2007).

The NLFFF extrapolation is performed in spherical geometry, however we lack the numerical libraries for computing Q in this geometry. Since the region is compact, we neglect the curvature of the photosphere and compute Q using existing software designed for Cartesian geometry (as in Savcheva et al. 2012a).

Furthermore, for the Q calculation, we interpolate the extrapolation magnetic field onto a grid that is uniformly spaced in all three Cartesian dimensions. The grid size is ≈ 0.36 Mm. The reference boundary for the Q computation, which defines the footpoint heights of each integrated field line, is chosen at $Z \approx 1.5\,\mathrm{Mm}$ to highlight the flux-rope related QSLs, and to exclude the QSLs related to small-scale polarities at the photosphere (cf. Savcheva et al. 2012a). In the following we refer to the plane at $Z \approx 1.5\,\mathrm{Mm}$ as the lower boundary. We compute the distribution of Q at the lower boundary and a vertical plane that cuts the flux rope.

The left panel of Figure 4 shows map of Q at the lower boundary. The dot-dashed

black line indicates the location of the vertical plane in which Q is computed and the corresponding map is displayed on the right panel of Figure 4. At the center of the horizontal plot, there are pronounced double inverse-J shaped QSLs that correspond to the main body of the flux rope, which may consist of different substructures like the different QSLs (the red , yellow, orange field lines in Figure 3). The straight sections (S+ and S-) coincide with the PIL, and the hook sections (H+ and H-) are located on either side of the PIL (H+ is located in the positive polarity and H- in the negative one). It is interesting to compare these QSLs to those derived from the TD flux rope shown **in** Figure 1. The QSLs in Figure 4 are hook shaped, but do not **completely encircle** the leg of the rope as in the panel (c) of Figure 1. It would appear that the flux rope obtain by the NLFFF extrapolation has a twist between 1 and 2 turns. This is comparable to the number of turns seen in Figure 2. The yellow arrows indicate hooked QSLs at the periphery that are parallel to the H+ and H- hooks. These are related to the field lines in yellow and orange in Figure 3. There are more external QSLs shown by the blue arrows. The QSLs represent the boundary between non sigmoidal active region connections and long remote field lines. They are not associated with the sigmoid.

The complex shape of the hooked QSLs with multiple arcs is reminiscent of a complex distribution of twist, more complex than in all the idealized models quoted in the Section 1, except for the magneto-frictional ones (Savcheva et al. 2012a) that are also complex.

The black arrow indicates another elongated QSL to the north of the PIL that encircles the positive polarity sunspot and stretches to the east. This QSL separates the field lines within the positive polarity into two systems. The southern system is a sheared arcade with relative low height in the vicinity of the flux rope (see the yellow field lines in Figure 3, panels (d) - (h)). The northern system overlays the flux rope (see the blue field lines in Figure 3, panels (g) and (h)).

We found the cross section of an inverse-drop QSLs volume (white dash line in heavy) in the HFT (indicated by the white arrow) in the right column of Figure 4. This inverse-drop QSLs defines the different quasi-connectivity between the flux rope and the overlaying arcades (the blue field lines in Figure 3, panels (g) and (h)). The height of the crossing section at HFT is relatively low and is considered to be the preferential place for reconnection (Aulanier et al. 2005; Janvier et al. 2013; Savcheva et al. 2012a,b, 2015).

The inverse-drop QSLs volume is relatively large, extending up to 25 Mm in height and with a similar width. This is in agreement with the size of the teardrop structure found in Savcheva et al. (2012a) and an order of magnitude larger than the one described in Zhao et al. (2014). This is another confirmation of the presence of a mature/well developed flux rope in the system. This teardrop topological structure is also embedded in larger weaker surrounding QSLs as previously described (Savcheva et al. 2012a; Guo et al. 2013). Another circular QSL (white dash line in light) is embedded inside the inverse-drop QSL, which demonstrates the different quasi-connectivity inside the flux rope, and confirms the complex distribution of twist in the flux rope. It is interesting to examine the correspondence between the field lines in Figure 3 and the QSLs in Figure 4. We find that the flux rope in Figure 3 (purple field lines) crosses the slice at Y $\sim$ 33 Mm and Z $\sim$ 25 Mm and does not pass through the small circle. The field lines that pass through the circle are longer and have a sigmoid shape similar to the orange field lines shown in Figure 3.

4.2. Comparison with Flare ribbons in the rising phase of the flare

Figure 5 shows a comparison between the QSL footprints at the lower boundary and the observed flare ribbons. The left column consists of AIA 304Å images showing the flare ribbons at different times during the eruption. The right column consists of the same AIA images with the QSL footprints superimposed.

The top row of Figure 5 shows brightenings develop well before the peak of the GOES X-ray flux at 17:45 UT. They have a similar shape as the double inverse-J shaped QSLs. Besides the brightening along these QSLs, there is also a faint one at the north-east along the elongated QSLs, at $(X, Y) \approx (50\,\mathrm{Mm}, 80\,\mathrm{Mm})$, the location is indicated by the black arrow in the top right panel. The right panels show the QSLs superimposed on the AIA image and demonstrate that the faint elongated brightening structure is the continuation (within the same polarity) of the intense, compact ribbon that forms at the north-west of the big sunspot later. The strong correlation between the brightening and the QSLs indicates that reconnection is occurring in the corona and the energy is transported along the 3D QSLs towards the footprints depicted in Figure 5 before the flare. Repeated brightenings are often observed (Cheng et al. 2015) and are interpreted as indicating that successive reconnection happens well before the impulsive phase of the flare.

While the GOES 1−8 Å soft X-ray light curve indicates that the flare begins at 17:21 UT, the UV observations shows that the evolution of the ribbons begins earlier. Between 17:05 and 17:21 UT, the hooked parts show zipping brightenings and their position evolves noticeably. Thus, the ribbons are very dynamic before the official start time of the flare at 17:21 UT. There is a relatively good agreement between the QSL footprints and the flare ribbons when they first appear at 17:05 UT. Some special features of the QSLs are labeled by arrows in the right column. The labels have the same meaning as those in Figure 4. We note an excellent match between the location and shape of the positive hook (H+) and the straight part of the negative ribbon (S-). Although the straight part of the positive ribbon (S+) is a few Mm north of the QSL, there is good agreement between the shapes. The negative hook (H-) also appears slightly shifted relative to the HFT footprint but, again, there is a good morphological agreement.

We expect that the two hours of difference between the time of the extrapola-

tion/topological analysis and the actual time of the flare is responsible for this small shift in location. We speculate that during that time the currents within the flux rope have grown and that the footprint of flux rope occupies a larger area, in particular in the more diffuse positive polarity. This can easily explain the difference of position between the QSL and H+.

To our knowledge, the present analysis shows the best match ever published between the position of the hooks of J-shaped flare ribbons and the topological analysis. With their extrapolation, Zhao et al. (2014, cf. Figure 10) were not able to capture the correct J shape of the observed ribbons. As discussed in Savcheva et al. (2015), the flux-rope insertion method was used to match seven different two J-shaped flares, the largest sample so far. They could recover well the straight part of the ribbons in all cases except for one involving a B-class flare. However, they were able to fit the hooked parts of the ribbons with the QSLs in only half of the studied regions and with an overall morphological agreement lower than in the present study. Since the flux-rope insertion method does not use vector magnetogram data, it is not as strongly constrained as the Grad-Rubin method. In addition, the magneto-frictional approach used in Savcheva et al. (2015) involves an ad hoc positioning of the extremities of a flux rope and the code is free to relax the foot points of the flux rope independently of the actual electric current concentrations. The excellent morphological agreement observed here between the position of the QSLs obtained solely from the extrapolation of magnetic information with fully independent UV observation at the onset of the flare, provides a clear demonstration of the quality of the extrapolation.

Between 17:05 and 17:21 UT, the brightenings at the hooks evolve rapidly. At 17:12 UT, the S+ ribbons moves further north and the H+ hook grows in size moving northward as well. On the contrary, the H- hook part appears to move inward towards the straight part S-. This tendency continues until 17:21 UT. Later during the flare, between 17:21 UT

and the peak phase of the flare at 17:45 UT, the hook parts H+ and H- appears to shrink, while stronger emissions originates from the straight parts S+ and S-.

While there was a good agreement between the QSLs from the NLFFF model and the flare ribbons when they first appear, the match becomes progressively worse as the eruption progresses, and the flare ribbons change their shapes and locations. In the framework of the CSHKP model in 2D, and of the recent standard model in 3D that results from MHD (Aulanier et al. 2012; Janvier et al. 2015) and magneto-frictional (Savcheva et al. 2016) simulations, these changes in the ribbons merely occur because of the ongoing flare reconnection during the eruption. Therefore it is natural that our static force-free model, which was constructed two hours before the eruption, no longer accurately represents the topology and therefore the ribbons on the long run. Thus, the hook parts of the sigmoidal structure in 304Å at the start of the eruption, and before the peak of the GOES flare, are recovered by our extrapolation because at this time the coronal magnetic field had not changed significantly from its force-free pre-flare state.

5. Discussion

We perform a NLFFF extrapolation of AR 12158 before a major eruption with the goal of testing the predictions of an eruptive flare model firstly proposed by Démoulin et al. (1996), then presented in a series of recent papers (Aulanier et al. 2012, 2013; Janvier et al. 2013) and reviewed in Janvier et al. (2015).

The authors refer to their model as "the standard flare model in three dimensions", which will also do in the following discussion. This model makes specific predictions regarding the topology of the pre-eruption magnetic field, which we test by performing a topological analysis of our extrapolated magnetic field.

The reliability of the topological analysis depends fundamentally on the reliability of the force-free extrapolation, so it is important to be mindful of the limitations of this kind of modeling. Generally, extrapolation methods perform better when applied to idealized test cases than to vector magnetogram data, which means that the results rely not only on the reliability of the extrapolation methods but also on the quality of the vector magnetograms (see the discussion in DeRosa et al. 2009).

A particular problem is that generally force-free methods do not achieve a self-consistent solution when applied to solar data, i.e. the extrapolation contains significant residual Lorentz forces. This is a problem for all methods, see for example the comparison of methods by DeRosa et al. (2009) and DeRosa et al. (2015). One specific advantage of the Grad-Rubin method, however, is that it is based on a well-posed formulation of the force-free boundary value problem and tends to satisfy the solenoidal condition ($\nabla \cdot \mathbf{B} = 0$) even when applied to solar data, while other methods may not (DeRosa et al. 2009).

The force-free extrapolation of AR 12158 encountered similar problems. We do not achieve a self-consistent solution because the Grad-Rubin did not strictly converge. We found that we could improve the convergence of our method either by excessive smoothing of the boundary, or by setting k to a small value. However, these solutions did not agree with the AIA images. The close agreement between the field lines of the less smoothed solutions and the AIA images indicates that the extrapolation likely reproduces the topology of the magnetic field. This is because the Grad-Rubin method does not specify a priori the connectivity of the field. For this study, this is more important than achieving a strictly force-free magnetic field by excessive smoothing of the boundary data. Nevertheless, it is important that the results presented here are considered with these caveats in mind.

The force-free model contains a clear magnetic flux rope as illustrated by the purple field lines in Figure 3. The appearance of the flux rope is similar to those obtained during

flux-cancellation MHD simulations of bipolar regions (Aulanier et al. 2012) – the overlying arcade, the twisted core, and the highly twisted S-shaped sigmoid appear in both cases.

We compute the squashing factor Q for the NLFFF extrapolation at the photosphere and a cross-section of the flux rope (see Section 4). The double inverse-J shaped QSLs at the photosphere, the inverse-drop QSLs and the HFT structure on the vertical plane found in our observation have been seen in both analytic models (Titov & Démoulin 1999) and MHD calculations (e.g., Aulanier et al. 2012). The appearance of an HFT in our extrapolation, which is non-idealized and based on real solar data, supports "the standard flare model in three dimensions" as a realistic model.

One interesting point from our extrapolation is the complex shape of the hooked QSLs, which wrap around the legs of the flux rope. Firstly they have multiple arcs which are almost parallel to each other at both ends of the flux rope. These features may be related with the multi-threaded curved ends of the sigmoid. Secondly, a QSL with a nearly circular cross-section is embedded inside the inverse tear drop shaped coronal QSL. These features all together tend to indicate that the twist distribution within the flux rope is much more complex in the extrapolation than in idealized models. The shapes of the inner hooked QSLs (H+ and H-) at the lower boundary (that are strongly curved and have a spiral-like shape), and those of the extrapolated field lines, both consistently show that the core of the flux rope in AR 12158 is more twisted than its envelope, and has between 1 and 2 turns.

We compare the distribution of Q on a plane $\approx 1.5\,\mathrm{Mm}$ above the photosphere to the flare ribbons. The QSLs on the plane closely match the flare ribbons at the start of the eruption. We note that the hook-shaped (J-shaped) extremities of the flare ribbons are recovered by the model and coincide with a QSL that wraps around the legs of the flux rope. This is consistent with the predictions of "the standard flare model in three dimensions" (Janvier et al. 2015). The nonlinear force-free model is an equilibrium state,

so it cannot be used to study the flare from its peak phase onwards.

6. Summary and conclusion

In this paper we successfully checked some predictions of "the standard flare model in three dimensions" (see Janvier et al. 2015) : the occurrence of double J-shaped QSL footprints below sigmoids ; their match with observed flare ribbons ; and their link with a coronal HFT. This result was obtained by performing a NLFFF extrapolation and a topological analysis of AR 12158, two hours before a sigmoid eruption and an X-class flare that took place on September 10, 2014.

The extrapolation was performed with the recently developed CFITS force-free modeling code in spherical geometry, that uses the Grad-Rubin method (Gilchrist & Wheatland 2014). Although the NLFFF model was calculated in spherical coordinates, we performed the topological analysis assuming a flat Cartesian geometry, by calculating the squashing factor Q with the QSL code developed by Zhao et al. (2014). This geometrical approximation has been used by others (e.g. Savcheva et al. 2015) who found that it only introduces minor errors for compact regions, such as AR 12158.

Among the various extrapolations that we produced, by varying several parameters of the method, we found one that produced a relatively good match between the sigmoid as observed with AIA and the modeled field lines. The extrapolated coronal field contains a magnetic flux rope, of which handedness also matches the observed inverse-S shape of the sigmoid. The distribution of the squashing factor Q at a plane $\approx 1.5\,\mathrm{Mm}$ above the photosphere revealed a double inverse J-shaped QSL footprint located on both sides of the polarity inversion line below the sigmoid. This is characteristic of coronal flux ropes. The complex hook-shaped extremities of the QSL footprint display a spiral-like shape. This is

reminiscent of idealized models of flux ropes of which core has slightly more than one turn. This is also consistent both with the field lines of modeled coronal flux rope itself, and with the distribution of Q as calculated in a coronal plane orthogonal both to the photosphere and to the flux rope axis, that reveals a closed quasi circular-shaped QSL embedded inside a larger flux-rope related inverse tear-drop shaped QSL, below which an HFT in present.

Several other observed features that are well reproduced by our extrapolation are worth noticing. Firstly, its vertical current density distribution at the photosphere resembles that derived from the HMI instrument, in particular in the plage flux concentrations where J_r was not prescribed as boundary conditions for the calculation. Secondly, we found a relatively good agreement between the QSLs of the model and the flare ribbons observed by AIA early in the flare, before its EUV/SXR peak, when the coronal field can still be represented by the pre-flare NLFFF. In particular, a surprisingly good match was achieved in the shape and location of the hook-shaped ribbons and QSL. Through its resulting QSL and HFT, our topological analysis straightforwardly explains why slip-running reconnection (Aulanier et al. 2007) occurred in this flaring active region, as previously reported by Li & Zhang (2015) and Dudik et al. (2016)

These agreements between the NLFFF model and the two independent sets of observations (AIA and HMI) firstly and fully confirm the aforementioned predictions of the "new standard flare model in 3D" (as compiled in Janvier et al. 2015). They are also consistent with results recently obtained with a different NLFFF code based on the magnetofrictional method (Savcheva et al. 2015, 2016). Secondly, they confirm the capacity of the Grad-Rubin method in general, in modeling solar sigmoids accurately, and in recovering thick coronal flux ropes (as previously achieved by Régnier & Amari 2004; Canou & Amari 2010). And thirdly, they support the quality of the CFITS code and of the methodology used in this paper, in particular, in their joint capacity in identifying key flux

rope properties, namely (i) their strong-to-weak twist distribution from its core to its outer parts, (ii) the location and extent of their photospheric endpoints, both of which being hard to obtain with other NLFFF methods, and (iii) the existence of a coronal HFT below the flux rope at the flare onset, that must lead to slip-running reconnection.

Following Savcheva et al. (2015), our results also support the claim that flare ribbons constitute one of the most complete sets of information that can be obtained on the geometry of erupting structures and on the sites of flare energy release, which are all together important elements of space weather studies. In this context, NLFFF models that can accurately reproduce the location and the shape of flare ribbons should henceforth result in reliable pre-eruptive flux rope properties, such as their magnetic twist, field strength, orientation, and free energy, as well as the location of its underlaying HFT. Such models may then be used not only to predict the location of the flare energy release through slip-running reconnection at the HFT, but also as initial conditions for MHD simulations of CME initiation and further propagation towards Earth.

The data have been used by courtesy of NASA/SDO and the HMI science team. SDO is a mission of NASA's Living With a Star program. We would like to thank P. Démoulin, J. Dudík and Y. Liu for fruitful discussions as well as the referee for helping us clarifying several points that were initially ambiguous. J. Zhao and H. Li are supported by the National Basic Research Program of China under grant 2011CB811402, by NSFC under grant 11273065, and by the Strategic Pioneer Program on Space Sciences, Chinese Academy of Sciences, under grant XDA04076101. J. Zhao is also supported by NSFC under grant 11503089, 11522328 and 11473070. Support for S.A. Gilchrist at LESIA was provided by a contract from the DIM ACAV and Région Ile-de-France. And his support at NWRA is provided by the NASA Living With a Star programthrough grant NNX14AD42G, and by the Solar Terrestrial program of the National ScienceFoundation through grant

AGS-1127327.

REFERENCES

Aly, J. J. 1989, Sol. Phys., 120, 19

Amari, T., Aly, J.-J., Canou, A., & Mikic, Z. 2013, A&A, 553, A43

Amari, T., Canou, A., & Aly, J.-J. 2014, Nature, 514, 465

Aulanier, G. 2014, in IAU Symposium, Vol. 300, IAU Symposium, ed. B. Schmieder, J.-M. Malherbe, & S. T. Wu, 184–196

Aulanier, G., Démoulin, P., Schrijver, C. J., et al. 2013, A&A, 549, A66

Aulanier, G., Janvier, M., & Schmieder, B. 2012, A&A, 543, A110

Aulanier, G., Pariat, E., & Démoulin, P. 2005, A&A, 444, 961

Aulanier, G., Pariat, E., Démoulin, P., & DeVore, C. R. 2006, Sol. Phys., 238, 347

Aulanier, G., Török, T., Démoulin, P., & DeLuca, E. E. 2010, ApJ, 708, 314

Aulanier, G., Golub, L., DeLuca, E. E., et al. 2007, Science, 318, 1588

Bobra, M. G., Sun, X., Hoeksema, J. T., et al. 2014, Sol. Phys., 289, 3549

Canou, A., & Amari, T. 2010, ApJ, 715, 1566

Canou, A., Amari, T., Bommier, V., et al. 2009, ApJ, 693, L27

Carmichael, H. 1964, NASA Special Publication, 50, 451

Chandra, R., Schmieder, B., Aulanier, G., & Malherbe, J. M. 2009, Sol. Phys., 258, 53

Cheng, X., Ding, M. D., & Fang, C. 2015, ApJ, 804, 82

Dalmasse, K., Aulanier, G., Démoulin, P., et al. 2015, ApJ, 810, 17

Démoulin, P., Priest, E. R., & Lonie, D. P. 1996, J. Geophys. Res., 101, 7631

DeRosa, M. L., Schrijver, C. J., Barnes, G., et al. 2009, ApJ, 696, 1780

DeRosa, M. L., Wheatland, M. S., Leka, K. D., et al. 2015, ApJ, 811, 107

Dudik, J., Polito, V., Janvier, M., et al. 2016, ArXiv e-prints, arXiv:1603.06092

Gilchrist, S. A., & Wheatland, M. S. 2014, Sol. Phys., 289, 1153

Gilchrist, S. A., Wheatland, M. S., & Leka, K. D. 2012, Sol. Phys., 276, 133

Golub, L., Deluca, E., Austin, G., et al. 2007, Sol. Phys., 243, 63

Gosain, S., Démoulin, P., & López Fuentes, M. 2014, ApJ, 793, 15

Grad, H., & Rubin, H. 1958, in Peaceful Uses of Atomic Energy, Vol. 31: Theoretical and Experimental Aspects of Controlled Nuclear Fusion, ed. J. H. Martens, L. Ourom, W. M. Barss, L. G. Bassett, K. R. E. Smith, M. Gerrard, F. Hudswell, B. Guttman, J. H. Pomeroy, W. B. Woollen, K. S. Singwi, T. E. F. Carr, A. C. Kolb, A. H. S. Matterson, S. P. Welgos, I. D. Rojanski, & D. Finkelstein (Geneva: United Nations), 190–197

Guo, Y., Ding, M. D., Cheng, X., Zhao, J., & Pariat, E. 2013, ApJ, 779, 157

Hirayama, T. 1974, Sol. Phys., 34, 323

Inoue, S., Hayashi, K., Magara, T., Choe, G. S., & Park, Y. D. 2015, ApJ, 803, 73

Janvier, M., Aulanier, G., & Démoulin, P. 2015, Sol. Phys., 290, 3425

Janvier, M., Aulanier, G., Pariat, E., & Démoulin, P. 2013, A&A, 555, A77

Kliem, B., Titov, V. S., & Török, T. 2004, A&A, 413, L23

Kopp, R. A., & Pneuman, G. W. 1976, Sol. Phys., 50, 85

Kosugi, T., Matsuzaki, K., Sakao, T., et al. 2007, Sol. Phys., 243, 3

Lemen, J. R., Title, A. M., Akin, D. J., et al. 2012, Sol. Phys., 275, 17

Li, T., & Zhang, J. 2014, ApJ, 791, L13

—. 2015, ApJ, 804, L8

Metcalf, T. R., Jiao, L., McClymont, A. N., Canfield, R. C., & Uitenbroek, H. 1995, ApJ, 439, 474

Pariat, E., & Démoulin, P. 2012, A&A, 541, A78

Pesnell, W. D., Thompson, B. J., & Chamberlin, P. C. 2012, Sol. Phys., 275, 3

Press, W. H., Teukolsky, S. A., Vetterling, W. T., & Flannery, B. P. 2007, Numerical Recipes 3rd Edition: The Art of Scientific Computing, 3rd edn. (New York, NY, USA: Cambridge University Press), 150

Priest, E. R. 1982, Geophysics and Astrophysics Monographs, Vol. 21, Solar Magnetohydrodynamics (Dordrecht; Boston: Reidel), 133

Régnier, S. 2013, Sol. Phys., 288, 481

Régnier, S., & Amari, T. 2004, A&A, 425, 345

Savcheva, A., Pariat, E., McKillop, S., et al. 2016, ApJ, 817, 43

—. 2015, ApJ, 810, 96

Savcheva, A., Pariat, E., van Ballegooijen, A., Aulanier, G., & DeLuca, E. 2012a, ApJ, 750, 15

Savcheva, A. S., van Ballegooijen, A. A., & DeLuca, E. E. 2012b, ApJ, 744, 78

Scherrer, P. H., Schou, J., Bush, R. I., et al. 2012, Sol. Phys., 275, 207

Schmieder, B., Aulanier, G., & Vršnak, B. 2015, Sol. Phys., 290, 3457

Schrijver, C. J., Aulanier, G., Title, A. M., Pariat, E., & Delannée, C. 2011, ApJ, 738, 167

Sturrock, P. A. 1966, Nature, 211, 695

Sun, X., Hoeksema, J. T., Liu, Y., et al. 2012, ApJ, 748, 77

Titov, V. S. 2007, ApJ, 660, 863

Titov, V. S., & Démoulin, P. 1999, A&A, 351, 707

Titov, V. S., Hornig, G., & Démoulin, P. 2002, Journal of Geophysical Research (Space Physics), 107, 1164

Török, T., Leake, J. E., Titov, V. S., et al. 2014, ApJ, 782, L10

van Ballegooijen, A. A. 2004, ApJ, 612, 519

Wang, Y., & Zhang, J. 2007, ApJ, 665, 1428

Wheatland, M. S., & Régnier, S. 2009, ApJ, 700, L88

Wheatland, M. S., Sturrock, P. A., & Roumeliotis, G. 2000, ApJ, 540, 1150

Wiegelmann, T. 2004, Sol. Phys., 219, 87

—. 2008, Journal of Geophysical Research (Space Physics), 113, 3

Wiegelmann, T., Inhester, B., & Sakurai, T. 2006, Sol. Phys., 233, 215

Wiegelmann, T., & Sakurai, T. 2012, Living Reviews in Solar Physics, 9, 5

Yang, K., Guo, Y., & Ding, M. D. 2015, ApJ, 806, 171

Yashiro, S., Gopalswamy, N., Akiyama, S., Michalek, G., & Howard, R. A. 2005, Journal of Geophysical Research (Space Physics), 110, A12S05

Zhao, J., Li, H., Pariat, E., et al. 2014, ApJ, 787, 88

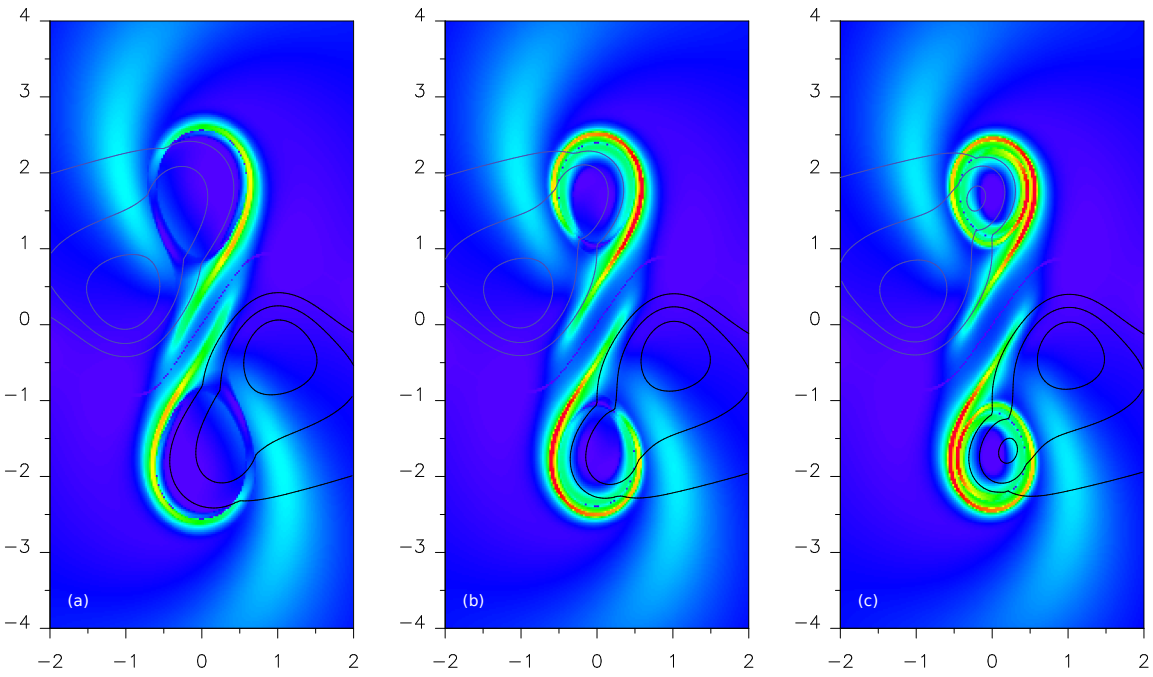

Fig. 1.— Photospheric QSL foot prints of the Titov-Démoulin flux rope model (Titov & Démoulin 1999) for different values of the flux-rope twist. The colour map shows the logarithm of the magnitude of the squashing factor Q. The QSLs are the region in red and yellow where Q is large. Panels (a) and (b) shows the hook-shaped QSLs of moderately twisted ropes with 1 and 1.5 turns respectively. Panel (c) shows the spiral-shaped QSLs of a highly twisted rope with a twist of 2 turns. The black and gray lines are contours of the normal component of the magnetic field.

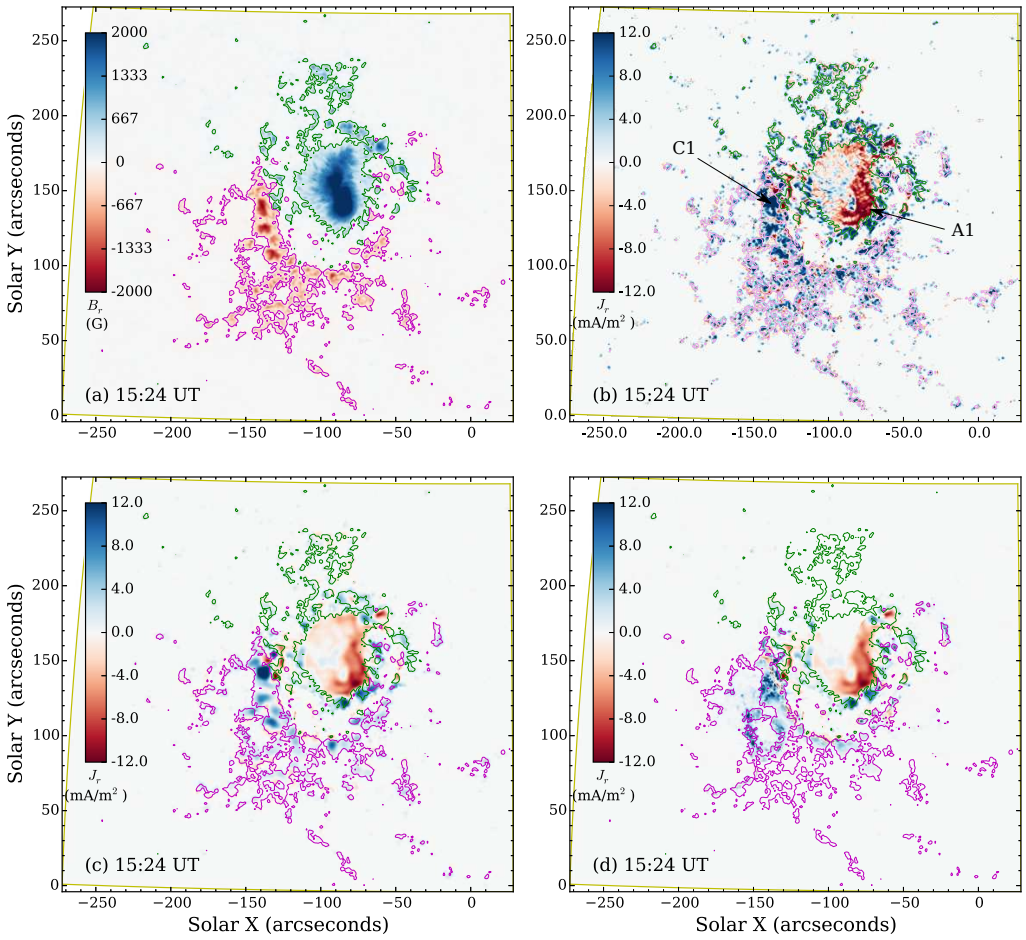

Fig. 2.— The photospheric boundary conditions for the NLFFF model of AR 12158. Panel (a) shows B_r. Panel (b) shows J_r computed from the HMI data without smoothing. Panel (c) shows J_r computed from the HMI data after first smoothing the transverse component of the magnetic field at the photosphere. This J_r is used to compute the α_0 boundary conditions for the force-free model. Panel (d) shows distribution of J_r from P solution of the nonlinear force-free model. Where $B_r < 0$ (inside the purple contours) the distribution of J_r is computed from the model rather than being fixed as a boundary condition (see Section 3). The purple and green lines are contours of B_r at ± 200 G respectively.

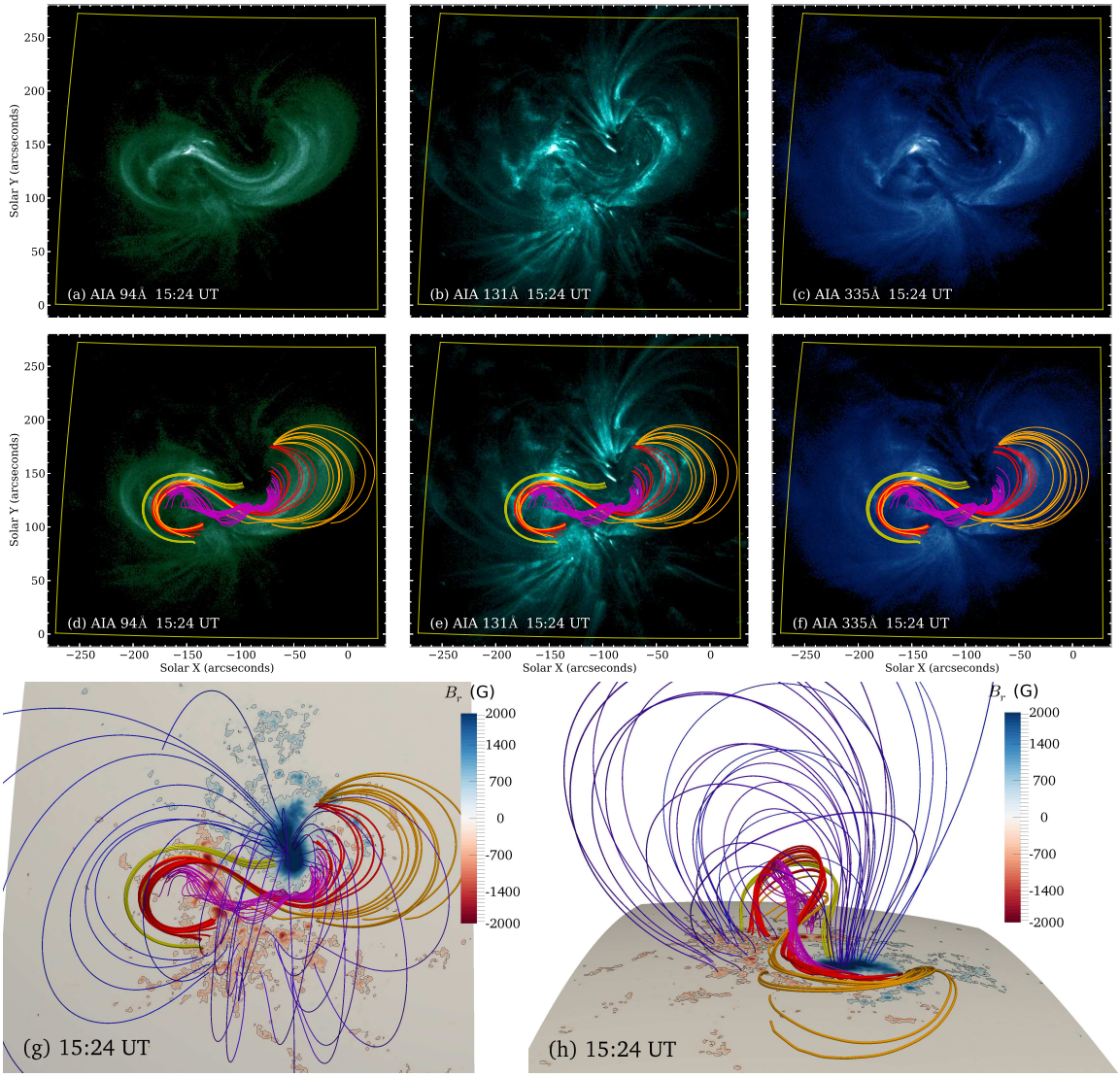

Fig. 3.— The coronal plasma of AR 12158 seen in EUV along with the field lines of the extrapolation. Panels (a)-(c) are AIA images of the region at 94Å 131Å and 335Å, respectively. Panels (d)-(f) are the same AIA images with selected field lines from the force-free model superimposed. Panels (g)-(h) are three-dimensional views of extrapolation field lines. Except for the blue field lines, which correspond to overlying arcades the field lines drawn in panels (d)-(e) are the same as those in panels (g)-(h). Panel (g) is a view of the region from the direction of Earth, and panel (h) is a view of the region looking towards solar east. The photosphere is coloured to show B_r, and the black lines are $B_r = \pm 200$G contours. The yellow region in panels (a)-(f) shows the photospheric extent of the calculation volume. The purple flux rope field has no observational counterpart in the AIA channels and in XRT image. The red, yellow and orange field lines trace the sigmoid.

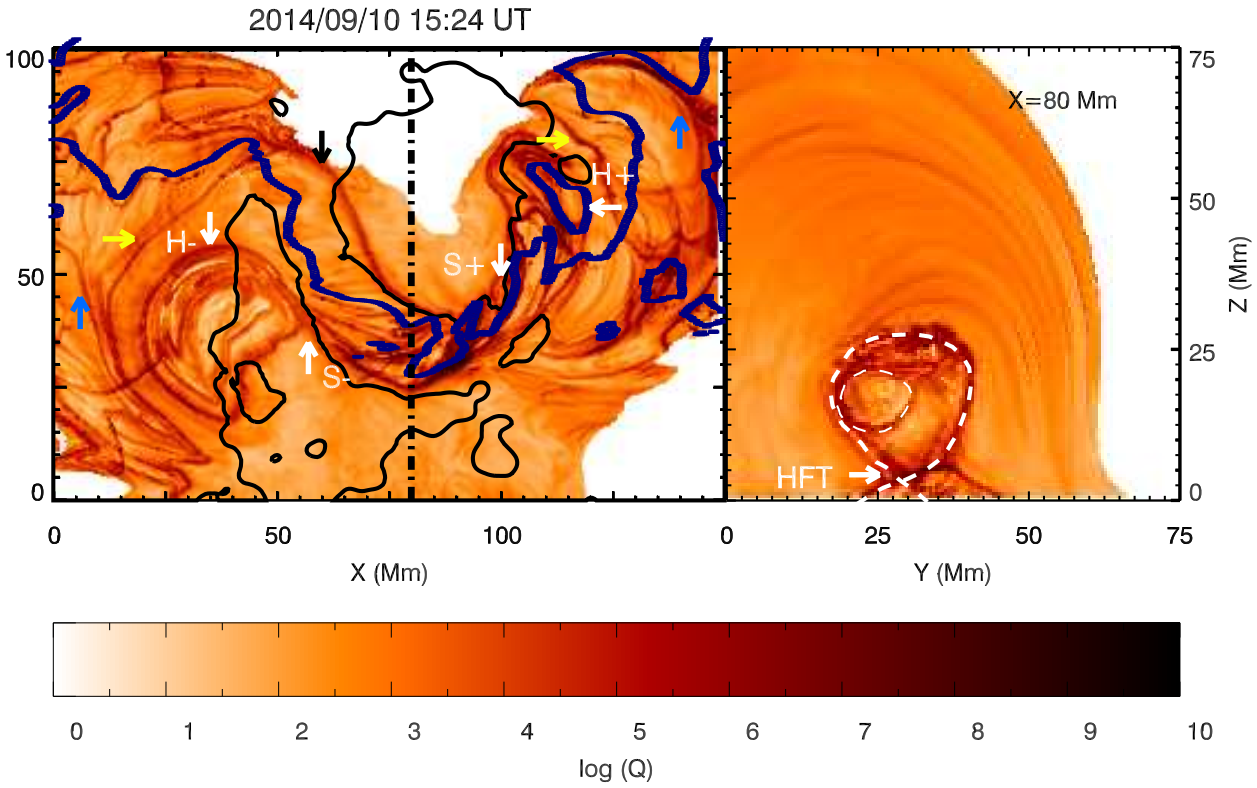

Fig. 4.— The left panel shows the distribution of the squashing factor Q at the photosphere at 15:24 UT (almost two hours before the X1.6 flare). The locations with relative high Q are the QSLs. The black curves are the ± 200 G contours of B_z, and the blue curve is the polarity inversion line. The white arrows show the four parts (H+, S+, H-, S-) of the double inverse-J shaped QSLs. The yellow arrows show the external QSL-hooks and the black arrow displays an elongated QSLs in the north of the PIL. The blue arrows indicate QSLs which separate the AR magnetic field with its environment. The vertical dot-dashed line shows the location of the slice cut shown in the right panel, where X equal 80 Mm. In the right panel, the dashed white line shows the inverse-tear drop-shaped envelope of the flux rope and the core of the flux rope in its middle, the white arrow indicates the location of the HFT structure.

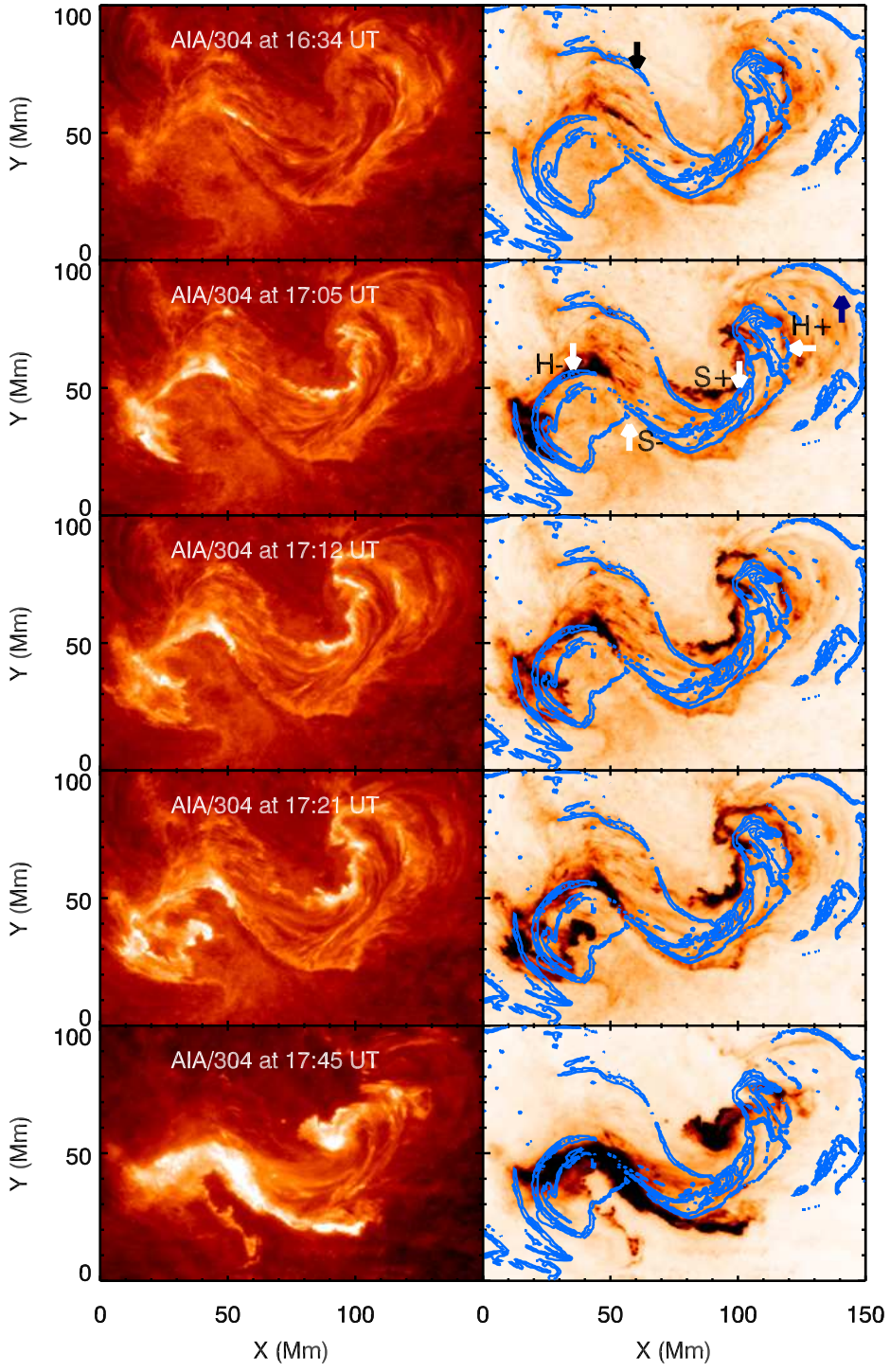

Fig. 5.— Flare ribbons as observed in 304 $\AA$ by AIA before and up to the peak of the flare (left and right columns, the latter in reverse color), and QSL footprints calculated from the single NLFFF extrapolation of the HMI magnetogram at 15:24 UT (right column, overplotted on all the 304 $\AA$ images). The arrows in the first two rows of the right column show the same structures of the QSLs being displayed on Figure 4.